PERGAMON

International Journal of Heat and Mass Transfer 46 (2003) 523–534

International Journal of HEAT and MASS TRANSFER

www.elsevier.com/locate/ijhmt

The effect of laser light propagation through a self-induced inhomogeneous process gas on temperature dependent laser-assisted chemical etching

James S. Hammonds Jr. [1], Mark A. Shannon *

University of Illinois at Urbana-Champaign, 140 M.E.B., 1206 West Green Street, Urbana, IL 61801, USA

Received 15 October 2001; received in revised form 21 June 2002

Abstract

High resolution and precise surface morphology is a primary goal of laser-assisted chemical etching (LACE) for microfabrication. However, the interaction of the laser light with the process gas can change the intensity incident to the target surface due to self-induced, thermally developed inhomogeneities within the gas. The exponential relationship between LACE rates and surface temperature means that very small changes in intensity, and thus surface temperature distribution, has a very large effect on the etch profile. This paper models both the inhomogeneous light–process gas interaction and the etching to predict the regimes in time and absorption path length where this effect needs to be considered. Numerical calculations of LACE microfabrication of borosilicate glass in a sulfur hexafluoride process gas with a 10.6 μm wavelength laser beam are given that show how the surface morphology of the glass wafer is changed by the inhomogeneous interaction.

1. Introduction

Over the last decade the use of lasers for microfabrication of polymers, metals and semiconductor materials has grown exponentially. Laser light is used to both deposit and etch materials. Often, in microfabrication, the laser light must pass through an ambient medium, such as a chemical process gas. Under these circumstances the laser's intensity field can cause local changes in the refractive index of the medium through which it is propagating. These local changes can, in turn, alter the intensity profile, and thus the evolution of the temperature at the surface. For laser-assisted chemical etching (LACE) in a process gas, the amount of material removed by chemical etching is a strong function of the surface temperature. Indeed LACE processes can be so highly sensitive to temperature that small changes in temperature can affect large changes in mass removal via etching.

In microfabrication via etching, the length scale of the etched feature is usually the property of interest. With LACE the goal is to obtain greater resolution with less surface roughness than that attained by thermal ablation or phase change. In order to do so, the laser intensity used is below the plasma ignition and explosive material removal threshold. Ideally, the fluence is also below that required to melt and evaporate the target material. However, even for laser beams at these relatively low intensities and short pulses (<1 ms), propagation through a process gas can significantly alter the intensity profile of the light from that desired, due to thermal interactions between the incident laser light and the process gas. These effects can introduce form errors in the etching as well as potentially increase surface roughness, both highly undesirable. Therefore, in this work, we investigate the affect of laser interactions with an absorbing gaseous medium on LACE.

* Corresponding author. Tel.: +1-217-244-1545; fax: +1-217-244-6534.

E-mail address: mas1@uiuc.edu (M.A. Shannon).

[1] Now at: City College of New York, Mechanical Engineering, New York 10031, USA.

0017-9310/03/$ - see front matter
PII: S0017-9310(02)00299-5

Nomenclature

a	absorption coefficient (m^{-1})
c	speed of light (m/s)
E	etch depth (m)
E_a	chemical activation energy (J)
Fo	dimensionless time
$Fo_{\Delta x}$	Fourier number
ΔG	Gibbs free energy (J/mol)
ΔG^*	dimensionless Gibbs free energy
ΔH	heat of formation (J/mol)
I	beam intensity (W/m^2)
$\hat{I}$	dimensionless beam intensity
K	equilibrium constant
k	wave number (m^{-1})
$\hat{k}$	dimensionless wave number
k_B	Boltzmann constant (J/mol K)
L	propagation length in medium 1 (m)
n	simple refractive index
$\hat{n}$	dimensionless refractive index
P	laser power (W)
$\hat{P}$	dimensionless laser power
R_0	rate constant (s^{-1})
R_u	universal gas constant (J/mol K)
r	reaction rate (s^{-1})
ΔS	entropy (J/mol K)
T	temperature (K)
t	time (s)
t_p	laser pulse width (s)
$\tilde{u}$	complex amplitude field (V/m)
u_c	characteristic amplitude field (V/m)
$\hat{u}$	dimensionless complex amplitude field
x, y	spatial directions perpendicular to laser beam propagation direction (m)
$\hat{x}, \hat{y}$	dimensionless spatial directions
$\Delta\hat{x}$	discretization size for $\hat{x}$ and $\hat{y}$ directions
z	laser beam propagation direction (m)
$\hat{z}$	dimensionless laser beam propagation direction
$\Delta\hat{z}$	discretization size for $\hat{z}$ direction

Subscripts

0	initial
1	medium 1
2	medium 2
c	characteristic
eff	effective
FS	free space
i, j, k	indices for x, y and z directions, respectively
in	effect of laser–material interaction included
s	surface of medium 2
Ref	reference
RXN	reaction

Superscript

p	index for time

Greek symbols

α	thermal diffusivity (m^2/s)
ε_0	free space permittivity ($C^2/N\,m^2$)
ε	characteristic dimensionless etch depth
κ	thermal conductivity (W/m K)
λ_0	central beam wavelength (m)
μ_0	free space permeability ($N\,s^2/C^2$)
σ_0	beam waist (m)
θ	dimensionless temperature
ζ	fraction of reactants

In general, LACE processes can involve electronic or vibrational excitation, or thermal heating of the solid and/or chemical etchant to induce a reaction. The mechanisms and applications of such processes have been investigated by several researchers [1–3]. We limit this work to time scales where thermal effects at the solid surface dominate chemical kinetics. For these cases it is necessary to calculate the surface temperature to characterize the etch process. Many workers have investigated methods of calculating the temperature of a surface heated by laser irradiation for the purposes of LACE, and related processes. With the assumption of constant material properties and one-dimensional heat flow, Burgess et al. [4] derives an analytical expression that describes the temperature at a solid surface. The beam is modeled as being uniform on the transverse plane, as having a triangular temporal pulse and as a surface heat source. Philippoz et al. [5] compares the results of [4] to a finite difference method that approximates the one-dimensional heat diffusion equation. This model accounts for temperature varying thermal properties, an experimentally determined laser pulse shape, and a spatially uniform intensity field that exponentially decays into the solid. The solutions compare well with experimental results and show the importance of considering temperature dependent properties when calculating heat transfer at the surface of a semiconductor. Diniz Neto et al. [6] employs an extension of this method, where the finite difference method is used to approximate the three-dimensional heat diffusion equation, including temperature varying thermal and optical properties. This model allows for Gaussian spatial and temporal profiles and shows the importance of considering thermally varying optical properties when calculating temperature profiles for metals. Methods involving integral transforms [7,8] have also been used

to solve for temperature change at a surface. However, all of the above models assume that the spatial profile, usually top hat or Gaussian, is maintained, and neglect the higher order effects of laser–material interactions in a process gas.

Thermally driven LACE can be viewed as consisting of three events: (i) laser beam propagation through the process gas, with a concurrent nonlinear laser–material interaction, (ii) laser heating of the solid surface via absorption and diffusion and (iii) the chemical reaction occurring at interface of the process gas and surface that produces the etched features of interest. We propose that for short pulsed lasers, the output intensity profile resulting from event (i) can be determined by combining the solutions of the paraxial wave and heat diffusion equations [9]. The output field from event (i) is then used as the energy generation term for (ii) in the heat diffusion equation, to solve for the temperature profile at the surface. Using this temperature profile we can then use an Arrhenius chemical rate equation for (iii) to calculate the etch depth profile at the surface. It should be noted that this form of the rate equation exponentially depends on the inverse temperature distribution, resulting in highly nonlinear etch depth dependence for even small changes in the temperature field caused by the inhomogeneous propagation of laser light through the process gas.

The purpose of this paper is to present the governing equations and the nondimensionalization utilized for this analysis. The results of this analysis are compared to models that neglect higher order laser-light interaction with the process gas to show that small variations in the temperature profile can result in significant changes in the etch profile. Results are also calculated and compared for varying dimensionless material properties of the process gas and laser and times. We then show similar results for the etch profiles that correspond to the temperature profiles. Finally, as a demonstration of the method, we present temperature variations and etch profile parameters for the specific case of laser-assisted dry etching of borosilicate glass (BSG) in sulfur hexafluoride (SF_6).

2. Theory

2.1. Laser beam propagation through process gas

This section will briefly present the governing equations used to predict the inhomogeneous laser light propagation through the process gas, along with the coupling equations. The method and its limits of validity, including the paraxial limitation, are described in detail by Hammonds et al. [9]. The physical system under consideration, and the co-ordinate axis used for this analysis is shown in Fig. 1. For laser beam intensities low enough such that higher order susceptibility

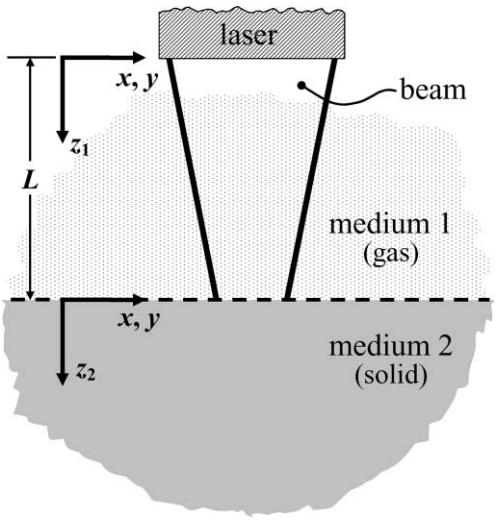

Fig. 1. Schematic illustrating the physical system under consideration and the co-ordinate axes used in the analysis, where the dashed line designates the medium interface. Section 2.1 describes a model for the laser–gas interaction occurring above the interface while Section 2.2 models the heat transfer resulting from laser irradiation taking place below the interface.

terms and Kerr effects are negligible, a paraxial wave equation is used, such that

$$\frac{\partial^2 \tilde{u}}{\partial x^2} + \frac{\partial^2 \tilde{u}}{\partial y^2} - 2jkn_0 \frac{\partial \tilde{u}}{\partial z_1} + k^2 \tilde{u}(n^2 - n_0^2) = 0, \tag{1}$$

where $\tilde{u}$ is the complex amplitude field, k is the wave number, n_0 initial refractive index, x and y indicates the beam's transverse directions and z_1 the propagation direction. The subscript 1 denotes propagation in medium 1 or the process gas. For laser pulses occurring over short times, but not so short as to produce significant pressure gradients within the medium, convection effects can be assumed negligible. Due to the low intensity laser light used in LACE, the process gas is assumed to be nonionized and sufficiently low enough in temperature to ignore radiative transfer. Thus energy absorption by the medium is assumed to occur via diffusion only. The field equation describing energy transfer is the heat diffusion equation

$$\frac{1}{\alpha_1}\frac{\partial T}{\partial t} = \frac{\partial^2 T}{\partial x^2} + \frac{\partial^2 T}{\partial y^2} + \frac{\partial^2 T}{\partial z_1^2} + \frac{a_1 I}{\kappa_1}, \tag{2}$$

where T is the temperature, α_1 is the thermal diffusivity of medium 1, κ_1 is the thermal conductivity, a_1 is the absorption coefficient, and I is the beam intensity. The imaginary component of the material complex refractive index is thus accounted for with a_1 as scattering of the laser light is assumed to be negligible [9,10]. Therefore the paraxial wave equation is coupled to the heat diffusion equation through a quadratic expression for the

real part of the refractive index, or simple refractive index

$$n^2(T) = n_0^2 + 2n_0 \frac{\mathrm{d}n}{\mathrm{d}T}\Delta T, \tag{3}$$

where $\Delta T = T - T_0$ and T_0 is the initial temperature. The heat diffusion equation is coupled to the amplitude by the expression for the intensity

$$I = 2n\left(\frac{\varepsilon_0}{\mu_0}\right)^{1/2} |\tilde{\boldsymbol{u}}|^2, \tag{4}$$

where $|\tilde{\boldsymbol{u}}|^2 = \tilde{\boldsymbol{u}}\tilde{\boldsymbol{u}}^*$, ε_0 is the free space permittivity, and μ_0 is the free space permeability.It should be noted that this analysis does not account for a true temporal profile. In this work, the beam's temporal shape is assumed to be a top hat for all cases. Accounting for temporal profiles is important when considering the maximum temperature rise at the surface. This analysis is interested in relative spatial profiles; thus the addition of this effect would not alter the qualitative results.

2.2. Laser heating of surface

The governing equations used to calculate the temperature distribution at the surface and within the volume are now presented. This analysis is limited to solid surfaces, where the temperatures are assumed to be low enough that changes in phases do not occur. In these cases the energy is transferred by diffusion. The analysis in Section 2.1 provides us with the laser's intensity distribution at the surface, $I(x, y, z_1 = L, t) = I(x, y, z_2 = 0, t) = I_s$ where L is the propagation distance in the process gas as shown in Fig. 1, and the subscript 2 denotes the solid sample. For a more thorough general analysis, temperature dependent optical and thermal properties should be included. Although addition of temperature varying thermal properties and absorption coefficients would not significantly change the qualitative results [5,6], reflected light at the surface could interfere with the incoming beam contributing to even greater changes in the intensity's spatial profile. This work neglects reflection, therefore this analysis should give a lower bound on the spatially varying thermal field. Heat diffusion in the solid is thus calculated with

$$\frac{1}{\alpha_2}\frac{\partial T}{\partial t} = \frac{\partial^2 T}{\partial x^2} + \frac{\partial^2 T}{\partial y^2} + \frac{\partial^2 T}{\partial z_2^2} + \frac{a_2 I_s \mathrm{e}^{-az_2}}{\kappa_2}, \tag{5}$$

where an exponential decay of the laser light into medium 2 is assumed for opaque targets.

2.3. Chemical reaction at interface

Here we present the equations that are used to predict the etch depth profile, for a given surface temperature profile. The processes of interest in this paper are those characterized by thermally mediated reactions at the surface, neglecting direct photochemical reactions. By integrating the reaction rate over time, the resulting etch depth can be determined. To model this portion of the process we assume that the reactions occur at the surface and that the rate, r, can be described by an Arrhenius type equation

$$r = R_0 \exp(-E_a/k_B T), \tag{6}$$

where the rate constant, R_0 is related to the density of the participating particles at the surface per unit time, E_a is the chemical activation energy, and k_B is the Boltzmann constant. In general, for processes where convection is negligible, R_0 can still vary with space and time. This effect can be due to diffusion induced by temperature gradients within the process gas or mass transfer due to changes in the particle density resulting from the surface reaction itself [11]. For this work we assume that the number of particles available to react remain constant for all space and time. Thus the etch depth resulting from a temperature profile at the surface is given as

$$E(x, y) = R_0 \int_0^{t_p} \exp(-E_a/k_B T(x, y, t))\mathrm{d}t. \tag{7}$$

This method was employed by Gold et al. [12] and Wautelet [13] to investigate reaction characteristics for LACE processes that included effects of temporally varying temperature fields. These works allow for thermal diffusion effects in the solid, however, the shape of the spatial intensity field was assumed constant for all times. In this work we seek to compare the qualitative differences between this and previous methods, thus only the relative shapes of the etch depth fields are important. It therefore suffices to deal with the equilibrium constant, K, which we estimate to be proportional to the rate, r, [14] or

$$r \sim K = \exp(-\Delta G/R_u T), \tag{8}$$

where ΔG is the Gibbs free energy of the reaction and R_u is the universal gas constant. With the local reaction rate, the etch depth, E, can be estimated as directly proportional to the reaction rate integrated over the pulse width or

$$\varepsilon = \frac{E(x, y)}{R_0} = \int_0^{t_p} \exp(-\zeta \Delta G(T(x, y, t))/RT(x, y, t))\mathrm{d}t, \tag{9}$$

where ζ is the fraction of reacting material and $\varepsilon = E/R_0$ is the dimensionless etch depth. This relationship allows for calculations of qualitative etch depth characteristics.

2.4. Nondimensionalization

To properly couple physical parameters between the laser beam, the process gas (medium1) and the solid

(medium 2), dimensionless parameters were developed. This section presents those parameters, which will ultimately generalize the results. The nondimensionalized governing equations that fully describe the LACE process will then be presented. Hammonds et al. [9] gives the nondimensionalization of the equations describing the laser process gas interaction as

$$\hat{x} = x/\sigma_0, \quad \hat{y} = y/\sigma_0, \quad \hat{z} = z/\sigma_0, \tag{10}$$

$$\theta = \frac{T - T_0}{T_0}, \tag{11}$$

$$\hat{k} = \sigma_0 n_0 k = \sigma_0 n_0 \frac{2\pi}{\lambda_0}, \tag{12}$$

$$\hat{n} = n/n_0 \tag{13}$$

and

$$\hat{u} = \tilde{u}/u_c, \quad u_c = \left[\frac{2P}{\pi\sigma_0^2}\left(\frac{\mu_0}{\varepsilon_0}\right)^{1/2}\right]^{1/2}, \tag{14}$$

where λ_0 is the central wavelength, P is the incident power, and σ_0 is the characteristic length associated with the optical beam, which we defined as the beam waist. The resulting dimensionless field equations describing laser propagation through the process gas are then given as

$$\frac{\partial^2\hat{u}}{\partial\hat{x}^2} + \frac{\partial^2\hat{u}}{\partial\hat{y}^2} - 2j\hat{k}\frac{\partial\hat{u}}{\partial\hat{z}_1} + \hat{k}^2\hat{u}(\hat{n}^2 - 1) = 0, \tag{15}$$

$$\hat{\nabla}^2\theta + \hat{I} = \frac{\partial\theta}{\partial Fo_1}, \tag{16}$$

$$\hat{n}^2(\theta) = 1 + 2\frac{d\hat{n}}{d\theta}\theta \tag{17}$$

and

$$\hat{I} = \hat{n}(\theta)\hat{P}|\hat{u}|^2, \tag{18}$$

where $Fo_1 = \alpha_1 t/\sigma_0^2$ and $\hat{P} = a_1 P/\pi\kappa_1 T_0$. Using these parameters, the dimensionless time for diffusion at the solid surface is given as

$$Fo_2 = \frac{\alpha_2 t}{\sigma_0^2} = \frac{\alpha_2}{\alpha_1}Fo_1 = \frac{1}{\alpha_R}Fo_1, \tag{19}$$

where the subscripts 1 and 2 denote the properties of medium 1 and medium 2 respectively, $\alpha_R = \alpha_1/\alpha_2$, and the governing equation is then given as

$$\hat{\nabla}^2\theta + \frac{\kappa_R}{a_R}\hat{I}e^{-a_2 z_2} = \alpha_R\frac{\partial\theta}{\partial Fo_1}, \tag{20}$$

where $\kappa_R = \kappa_1/\kappa_2$ and $a_R = a_1/a_2$. Finally, etch depth characteristics are determined with a form of Eq. (9)

$$\varepsilon(x,y) = \int_0^{Fo_1^p} \exp(-\zeta\Delta G^*/(\theta+1))\mathrm{d}Fo_1, \tag{21}$$

where $\Delta G^* = \Delta G/T_0 R_u$ and $Fo_1^P = a_1 t_p/\sigma_0^2$, and ζ is defined in Section 4.

3. Computations

3.1. Computational method

This section gives the computational methods employed to obtain solutions for the equations presented above. The computational method used to calculate solutions for the laser spatial output intensity field follows that of Hammonds et al. [15], where Eqs. (15) and (16) are approximated using the finite difference method. A brief summary of this method is provided here. To maintain stability and to achieve solutions with greater accuracy at lower computational cost than those obtained by straightforward implicit methods, the paraxial wave equation is modeled using the Crank–Nicholson method with a predictor–corrector implementation. To achieve the required accuracy, small time steps are required due to the nonlinear nature of the diffusion equation when coupled to the wave equation. Larger steps would require that implicit methods iterate a considerable number of times, using more floating point operations than an explicit method would. An explicit finite difference scheme is therefore used to solve Eq. (16), maintaining the appropriate stability requirement. These equations are coupled by the explicit discrete forms of Eqs. (17) and (18). The reader is referred to Ref. [15] for a more detailed description of this method.

The finite difference method is also used to approximate the heat diffusion equation, to model heat transfer in the bulk of medium 2, resulting from event (ii). Following the method of [4] and [15] Eq. (20) is solved explicitly as

$$\begin{aligned}\theta_{i,j,k}^n = {} & \frac{Fo_{\Delta x,1}}{\alpha_R}(\theta_{i+1,j,k}^{n-1} + \theta_{i-1,j,k}^{n-1} + \theta_{i,j+1,k}^{n} + \theta_{i,j-1,k}^{n-1} \\ & + \theta_{i,j,k+1}^{n} + \theta_{i,j,k-1}^{n-1}) + \left(1 - 6\frac{Fo_{\Delta x,1}}{\alpha_R}\right)\theta_{i,j,k}^n \\ & + \frac{\kappa_R}{a_R}\hat{I}_{i,j,k=0}^n \exp(-a_2 k\Delta\hat{z}),\end{aligned} \tag{22}$$

where i, j, and k are indices for the x, y, and z directions, respectively, $\Delta\hat{x}$ is the discretization size in the x and y directions, $\Delta\hat{z}$ in the propagation direction and n is the index for time, $Fo_{\Delta x,1}$, with the stability criteria given as

$$Fo_{\Delta x,1} = \frac{Fo_1}{(\Delta\hat{x})^2} \leqslant \frac{\alpha_R}{6}. \tag{23}$$

An expression is then derived to calculate heat transfer at the surface boundary. This expression is derived noting that the transverse beam dimension is much larger than the absorption depth at the surface or $\sigma_0 \gg a_2^{-1}$, allowing for one-dimensional analysis at the surface. An

energy balance applied to the surface of medium 2 is used to derive the FD equation at the interface (assuming negligible reflection) as

$$\theta^n_{i,j,s} = Fo_{\Delta x,\mathrm{eff}}(\kappa_R\theta^{n-1}_{i,j,s+1} + \theta^{n-1}_{i,j,s-1}) + (1 - Fo_{\Delta x,\mathrm{eff}}(\kappa_R + 1))\theta^n_{i,j,s} + Fo_{\Delta x,\mathrm{eff}}\frac{1}{2}\left(1 + \frac{1}{a_{\mathrm{rat}}}\right)\kappa_R\hat{I}^n_{i,j,s}, \quad (24)$$

where the subscript s denotes the surface node, with

$$Fo_{\mathrm{eff}} = \left[\frac{1}{2}\left(\frac{\kappa_R}{Fo_1} + \frac{1}{Fo_2}\right)\right]^{-1} \quad (25)$$

and the surface stability criteria given as

$$Fo_{\Delta x,\mathrm{eff}} = \frac{Fo_{\mathrm{eff}}}{(\Delta\hat{x})^2} \leqslant \frac{1}{(\kappa_R + 1)}. \quad (26)$$

Finally, a quadrature algorithm, implemented through the use of MATLAB is used to calculate $\varepsilon(i\Delta x, j\Delta y)$ at the surface using Eq. (21). This method uses an adaptive recursive Newton–Cotes 8 panel rule.

3.2. Computational procedure

This section outlines the implementation of the computational method discussed above. SGI's Origin2000 parallel supercomputer was used for these calculations in the following manner. We first calculate solutions from the model that describes the laser material interaction. This output is an amplitude field, which is then used as the source term for the heat diffusion process in the solid. The result of this analysis is a temperature field at the solid surface. This temperature distribution is then used with the algorithm that allows us to determine the etch depth characteristics.

The computational procedure to solve laser–process gas interaction in medium 1 is as follows. This problem is initialized ($p = 1$) with a known intensity field—the output from the laser cavity, propagating undisturbed through space. This initial intensity field, $(\hat{I}^{p=1}_{i,j,k})_{\mathrm{med1}}$, is discretized over the entire domain of medium 1, such to conform to the spatial grid. This intensity field is then used with the explicit FD expression for Eq. (16) to calculate the temperature field, $(\theta^{p=1}_{i,j,k})_{\mathrm{med1}}$, throughout the domain. This temperature is then used with the explicit FD form of Eq. (17) to calculate the refractive index, $(\hat{n}^{p=1}_{i,j,k})_{\mathrm{med1}}$. Next, by using the refractive index field with the implicit FD approximation of Eq. (15) the new amplitude, $(\hat{u}^{p=2}_{i,j,k})_{\mathrm{med1}}$, is determined. Finally, a new intensity field, $(\hat{I}^{p=2}_{i,j,k})_{\mathrm{med1}}$, is calculated by using the explicit FD approximation of Eq. (18). This process is repeated over the entire domain of medium 1 until the desired time step is reached. For a more detailed description and the procedure used to parallelize the code, the reader is referred to [15].

As previously mentioned, the boundary of medium 1, $z_1 = L$, is the boundary for medium 2, $z_2 = 0$. Thus the final output intensity field recovered from the previous analysis provides the source term for the surface temperature calculations or, $(\hat{I}^p_{i,j,k=L})_{\mathrm{med1}} = (\hat{I}^p_{i,j,k=0})_{\mathrm{med2}}$. For these calculations, $(\hat{I}^p_{i,j,k=0})_{\mathrm{med2}}$ is used with Eqs. (22) and (24) to determine $(\theta^p_{i,j,k=0})_{\mathrm{med2}}$ for all times. This method was also parallelized using the methods of [15]. With a surface temperature field distribution, the characteristics of the etch pattern can be calculated with the use of Eq. (21). This analysis first requires a value for the Gibbs free energy, ΔG^* which is determined using the thermochemical data obtained from Ref. [16] for the rate limiting reaction (cf. Eq. (27c)) discussed in Section 4. Using the temperature dependent values for ΔG^* (cf. Eq. (28)) and the temperature distribution at the surface, MATLAB code was written to solve Eq. (21).

4. Results

In other research, the solutions were obtained by assuming the beam spatial profile could be described as a Gaussian or top hat for all times. The current work shows that at certain pulse times and beam fluences this assumption could be invalid, depending on the material properties. We show this by comparing surface temperatures calculated with beam interaction with the process gas included in the analysis, θ_{in} to results obtained assuming free space beam propagation, θ_{FS}. In many cases of interest, the variations in these results may appear small, but the manifestation of these changes in the etch depth characteristics can be considerable. We show this by comparing the etch depth calculated with θ_{in} or $\varepsilon_{\mathrm{in}}$ to results calculated with θ_{FS} or $\varepsilon_{\mathrm{FS}}$ for ranges of Fo_1, a_1L, and $\hat{I}/\hat{I}_{\mathrm{Ref}}$.

Fig. 2 shows the variation of $\theta_{\mathrm{in}}/\theta_{\mathrm{FS}}$ with increasing Fo_1. In these calculations, the parameter, a_1L is set to 2, a constant, where relatively modest departure from the free space temperature solution is noted (cf. Fig. 4). The parameter $\theta_{\mathrm{in}}/\theta_{\mathrm{FS}}$ is important in quantifying the difference between solutions accounting for higher order effects and solutions that neglect them. For early times, or low Fo_1 the plot is basically planer, with slight variations occurring near the middle of the time span and more significant hills ($\theta_{\mathrm{in}}/\theta_{\mathrm{FS}} > 10$) and valleys ($\theta_{\mathrm{in}}/\theta_{\mathrm{FS}} > 0.5$) at later times. It is obvious that the great variations observed at later times would contribute to significant errors in an analysis assuming a constant beam profile, but the small variations should be considered as well. This point is exemplified in Fig. 3 where $\varepsilon_{\mathrm{in}}/\varepsilon_{\mathrm{FS}}$ is plotted against the varying Fo_1. Similar behavior is observed in both figures, characterized by initially small changes growing into significant changes. However, changes in Fig. 3 occur rapidly, as to be expected by the exponential behavior of the Arrhenius

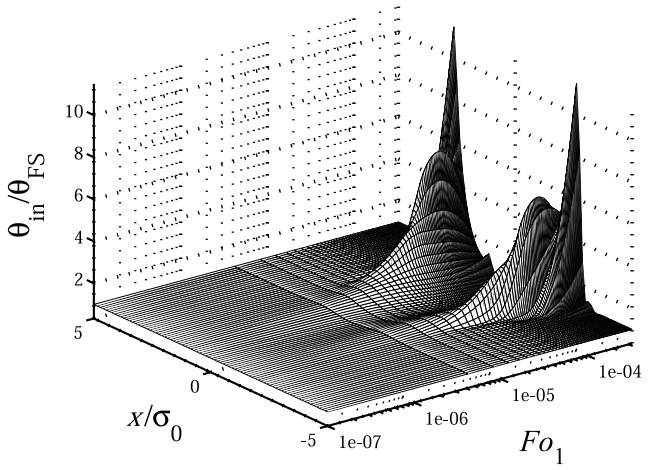

Fig. 2. Variation of θ_{in}/θ_{FS} with Fo_1 where the quantity θ_{in}/θ_{FS} represents the difference in surface temperature calculations that include higher order beam propagation effects, θ_{in}, and those that neglect these effects, θ_{FS}, and Fo_1 is the nondimensional time in the analysis. For this analysis $a_1L = 2$ and $\hat{I}/\hat{I}_{Ref} = 2$. This plot shows that for short times, variations are small. However, these small differences in the temperature result in a considerable change in the etch field as shown in Fig. 3

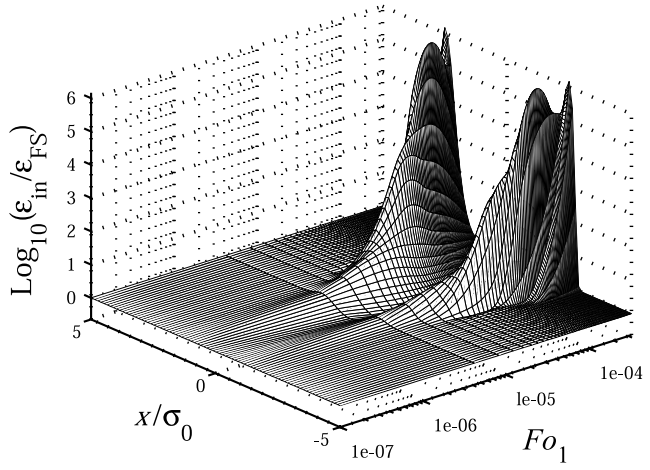

Fig. 3. Variation of $\varepsilon_{in}/\varepsilon_{FS}$ with Fo_1 where the quantity $\varepsilon_{in}/\varepsilon_{FS}$ represents the difference in surface etch depth calculations that account for higher order beam propagation effects, ε_{in}, and those that neglect these effects, ε_{FS}, and Fo_1 is the nondimensional time in the analysis. For this analysis $a_1L = 2$ and $\hat{I}/\hat{I}_{Ref} = 2$. The small temperature variations shown in Fig. 2, results in several orders of magnitude differences in etch depth. These results suggest that higher order beam effects could be important for calculations of certain LACE processes.

equation. In fact, in comparing Figs. 2 and 3, we see that for the same Fo_1 of 10^{-5}, variations of the temperature field are on the order of one, whereas variations in the etch depth field are on the order of ten.

Similar behavior is observed when variations of θ_{in}/θ_{FS} and $\varepsilon_{in}/\varepsilon_{FS}$ are plotted against a changing absorption parameter, a_1L, while Fo_1 is held constant at 5×10^{-5}. Fig. 4 shows the changes in θ_{in}/θ_{FS} with respect to an increasing a_1L. These variations in temperature are characteristically similar to Fig. 2. One would expect qualitative behavior to be consistent because the source term in the diffusion equation increases linearly with an increasing absorption coefficient and time. Fig. 5 shows how $\varepsilon_{in}/\varepsilon_{FS}$ varies with a_1L. The fact that changes in temperature on the order of one can contribute to changes of orders of ten in the etch depth is evident in this plot as well. The deviations in etch depth shown in Fig. 5 differ by several orders of magnitude from those shown in Fig. 3 however. This is because of the shorter laser pulse width involved in the etch calculations used

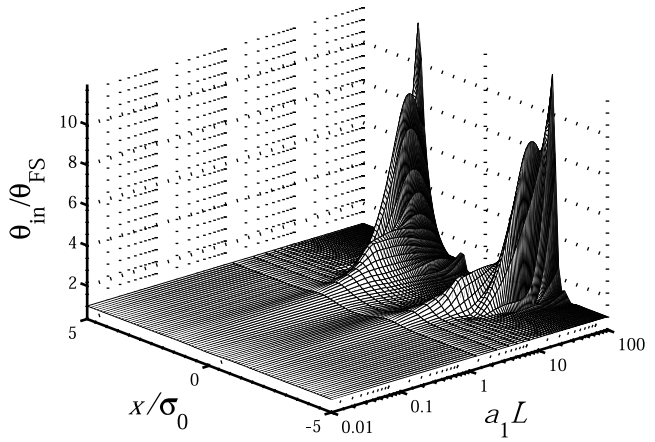

Fig. 4. Variation of θ_{in}/θ_{FS} with a_1L, where the quantity θ_{in}/θ_{FS} represents the difference in surface temperature calculations that include higher order beam propagation effects, θ_{in}, and those that neglect these effects, θ_{FS}, and a_1L is the nondimensional absorption coefficient of the process gas. For this analysis $Fo_1 = 5 \times 10^{-5}$ and $\hat{I}/\hat{I}_{Ref} = 2$. These results are consistent with those shown in Fig. 2, large differences in the temperature fields only occur for large absorption coefficients. However, the small variations for the midrange values of a_1L translate into significant differences in the etch depth, as shown in Fig. 5.

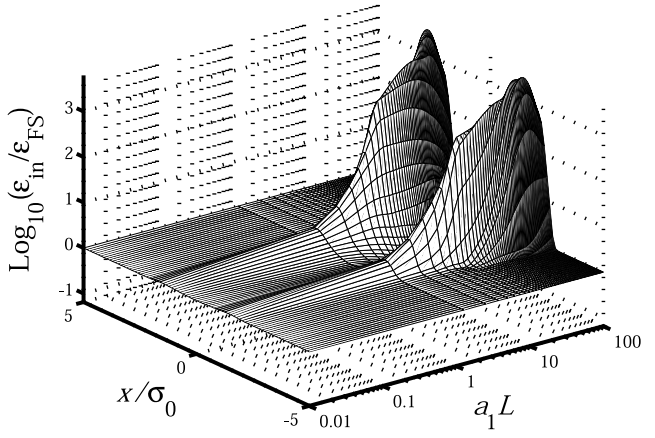

Fig. 5. Variation of $\varepsilon_{in}/\varepsilon_{FS}$ with a_1L, where the quantity $\varepsilon_{in}/\varepsilon_{FS}$ represents the difference in surface etch depth calculations that account for higher order beam propagation effects, ε_{in}, and those that neglect these effects, ε_{FS}, and a_1L is the nondimensional absorption coefficient of the process gas. For this analysis $Fo_1 = 5 \times 10^{-5}$ and $\hat{I}/\hat{I}_{Ref} = 2$. The evolution of these etch field differences with a_1L is consistent with the results shown in Fig. 3. The small variations in the temperature fields shown in Fig. 4 cause major changes in the etch fields.

in Fig. 3. Figs. 3 and 5 show that for larger absorption, etch profile changes resulting from increases in Fo_1 and a_1L compound, making possible extremely large deviations from the free space solution for given laser intensities.

Although, many simplifications have been made in modeling these LACE processes, we believe the results to be qualitatively descriptive in demonstrating that neglecting higher order effects in laser propagation through a participating medium can, in some cases, result in significant modeling errors. Moreover, including effects of a varying reactant density at the surface would introduce more nonlinearities into the solution [11,17], contributing to even greater variations.

The above analysis provides us with the degree of variation between results that include higher order laser effects and those that ignore them, however, a clear representation of the actual etch depth field is not presented. This information is of great importance for LACE processes where the goal is precise microfabrication. For this purpose we investigate the specific case of laser-induced dry etching of BSG ($B_2O_3 + SiO_2$) in a

sulfur hexafluoride (SF_6) process gas. The Gibbs free energy, ΔG, for the reaction is determined for BSG composed of 84% SiO_2 and 16% B_2O_3 by weight by assuming that the process can be described as three reactions:

$$SiO_2 + 2SF_6 \rightarrow SiF_4 + 2SF_4 + O_2 \quad (27a)$$

$$B_2O_3 + 3SF_6 \rightarrow 2BF_3 + 3SF_4 + (3/2)O_2 \quad (27b)$$

$$SiO_{1.51} + 2SF_6 \rightarrow SiF_4 + 2SF_4 + (1.51/2)O_2 \quad (27c)$$

and using [18]

$$\Delta G_{RXN} = \Delta H_{RXN} - T\Delta S_{RXN} \quad (28)$$

where ΔH_{RXN} is the heat of formation of the reaction and ΔS_{RXN} is the entropy. Fig. 6 plots the variation of ΔG_{RXN}, for each reaction, with temperatures varying from room temperature to the approximate melting temperature of BSG. This plot shows that reactions 1 and 2 have little chance of occurring under 450 K, while ΔG_{RXN} is very negative for reaction 3 at all temperatures. Above 450 K, reaction 2 has a greater chance of reacting than 1, and thus from Fig. 6 we can conclude that reaction 2 occurs faster than 1. Furthermore, noting that Eq. (27c) represents a reaction that occurs after the partial reduction of the borosilicate, and that this reaction occurs much faster than reaction 2, we conclude that Eq. (27b) is the rate limiting reaction. This value for the Gibbs free energy of Eq. (27b) is used with Eq. (21) where ζ is defined as

$$\zeta = \frac{\Delta G_{RXN3}}{\Delta G_{RXN3} + \Delta G_{RXN2}}. \quad (29)$$

Fig. 7 shows the surface temperature distribution, θ_{in}, for varying values of $\hat{I}/\hat{I}_{Ref}$. In this case $\hat{I}_{Ref} = 3 \times 10^3$ which, for the specific case of dry etching of BSG with SF_6 with a beam of spot size 1 mm^2, would give an intensity of the order 10^6 {W/cm^2}, well below the ablation threshold of BSG. The material properties used in this analysis are presented in Table 1. For this analysis Fo_1 is held constant at 5×10^{-5}, thus this figure represents the surface temperature after being heated for this time span over varying $\hat{I}/\hat{I}_{Ref}$. For large Fo_1 the results become singular and method is no longer valid. In this figure, the temperature distribution which is Gaussian initially takes a parabolic form for low $\hat{I}/\hat{I}_{Ref}$. As the intensity is increased, the fluid in which the laser is propagating heats up causing the beam profile to deviate from a Gaussian. Diffusion effects within the solid smooth out these deviations at lower intensities, broadening and flattening the previously parabolic distribution. As the intensity increases even higher, these beam deviations begin to manifest themselves in the temperature profile as peaks on the outer edges. These peaks increase and new ones form as the beam profile filaments due to the laser–process gas interaction. The etch depth, ε_{in}, corresponding to the temperature profile shown in Fig. 7 is presented in Fig. 8. The logarithmic of this etch depth is presented to clearly show the variation in etch depth as the intensity increases. The etch depth profile is smooth for low intensities, which is desirable for fabrication processes. As this intensity increases, peaks form on the outer edges and, in fact, they begin to dominate. At greater Fo_1 the etch profile would deviate greatly from the initial Gaussian profile. An example

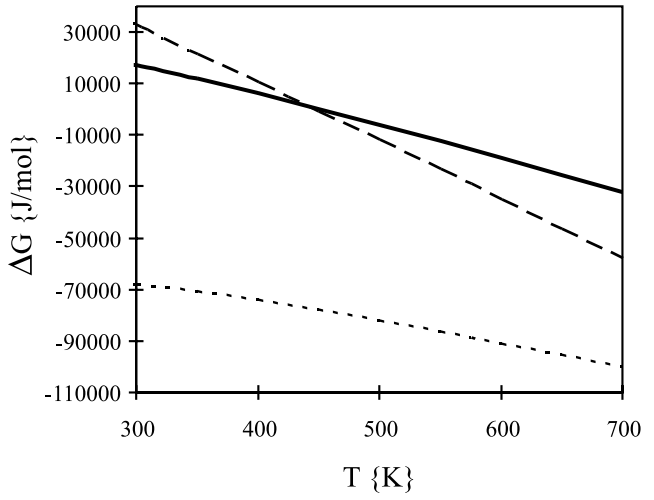

Fig. 6. The change in $\Delta G^*_{RXN}R$ with $T_0(\theta + 1)$ for three competing reactions: $SiO_2 + 2SF_6 \rightarrow SiF_4 + 2SF_4 + O_2$ (—), $B_2O_3 + 3SF_6 \rightarrow 2BF_3 + 3SF_4 + (3/2)O_2$ (- - -) and $SiO_{1.51} + 2SF_6 \rightarrow SiF_4 + 2SF_4 + (1.51/2)O_2$ (···). From this plot it is estimated that, in the etching of BSG by SF_6, reaction 2 rate limiting, as reaction 1 occurs slower at high temperatures and reaction 2 occurs much faster.

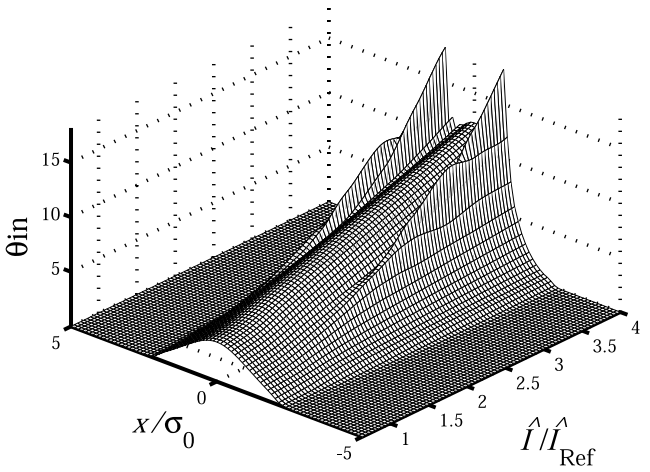

Fig. 7. The change in the nondimensional temperature, θ_{in}, with $\hat{I}/\hat{I}_{Ref}$, over a time period of $Fo_1 = 5 \times 10^{-5}$, where x/σ_0 is the transverse spatial plane. This analysis is for the dry etching case of BSG in SF_6, using material properties shown in Table 1. The temperature distribution is Gaussian for low intensities, but as laser fluence increases the distribution gradually changes to reflect the changes in the spatial distribution of the intensity field. At midrange intensities, peaks that are formed by the altered intensity field are accompanied by broadening due to diffusion. At high intensities these peaks dominate.

Table 1
Thermal and optical properties used in modeling dry etching of BSG in sulfur hexafluoride

	SF_6	$SiO_2 + B_2O_3$
Absorption coefficient (m^{-1})	35.50[a,b] [19]	1.05×10^{6}[c] [22]
Thermal conductivity (W/m K)	0.013[b] [20]	1.00[b] [21]
Density (kg/m^3)	6.164[b] [20]	
Specific heat (J/kg K)	666.0[b] [21]	719.0[b] [21]
Thermal diffusivity (m^2/s)		5.50×10^{-7}[b] [21]

[a] Laser wavelength 10.6 nm.
[b] At 1 atm, 300 K.
[c] Laser wavelength 10 nm.

LACE process that supports the computational results obtained in this work is shown in Fig. 9 (taken from Ref. [23]). The SEM micrograph in this figure shows the fabricated features on a Ni (80%)–Fe (20%) alloy, etched in an atmosphere of CCl_4 at 100 Torr with a 6.3 W Gaussian Ar laser beam for 120 s. With the spot size of 80 μm, the intensity is estimated as 125 kW/cm^2. The resulting etch profile does not match the incident Gaussian laser intensity profile, possibly because thermally induced inhomogeneities within the gas brought about a temperature distribution that is higher at the hole edges and lower at the center. This situation, similar to that plotted in Fig. 7, results in an etched depth that is deeper at the edges, such as shown in Fig. 8. Other researchers report that absorption of Ar laser light by liquid CCl_4 gas does not exceed 0.01% and is therefore negligible when examining similar LACE systems [24]. However, for the relatively long exposure time used to produce the etch pattern shown in Fig. 9, absorption coefficients as low as 1×10^{-8} (cm^{-1}) are estimated using Eq. (2.15) of Ref. [10] to be sufficient to drive temperature changes on the order of 0.1%. These temperature changes are enough to significantly change laser beam focal characteristics [9], and therefore the etch depth.

The work presented here outlines a procedure for calculating the surface temperature for the purpose of LACE processing. This model takes into account the spatially varying laser intensity of a laser propagating through a thermally participating medium. We show that accounting for these effects may be necessary by calculating the etch depth field produced in these processes. Results from the etch depth calculations show that small differences between temperature field calculations that account for laser–material interactions and those that do not could translate into significant differences in the predicted etch field. For low absorption coefficients, small pulse widths and low intensities, higher order effects from laser–material interactions are negligible, but when these properties become large, the effects of beam propagation in the inhomogeneous medium dominate. This work presents qualitative results for a range of these parameters, and results for the specific case of dry etching BSG in SF_6. A thorough

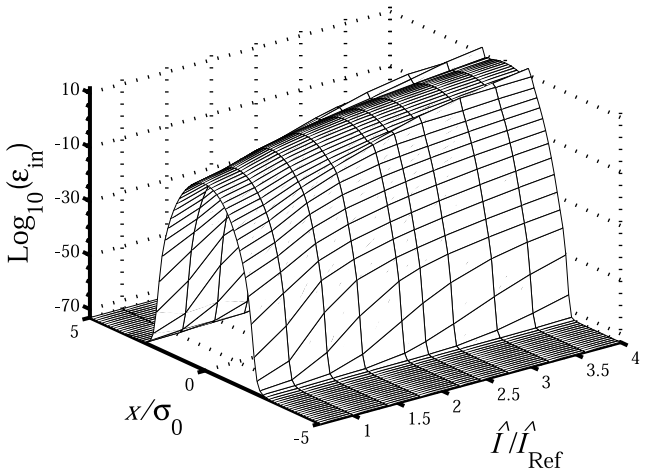

Fig. 8. The change in the characteristic etch depth, ε_{in} with $\hat{I}/\hat{I}_{Ref}$, over a time period of $Fo_1 = 5 \times 10^{-5}$, where x/σ_0 is the transverse spatial plane. This analysis is for the dry etching case of BSG in SF_6, using material properties shown in Table 1. At the midrange intensities on this plot, peaks consistent with those that appear in the temperature field shown in Fig. 7. At high intensities these peaks dominate the characteristic shape.

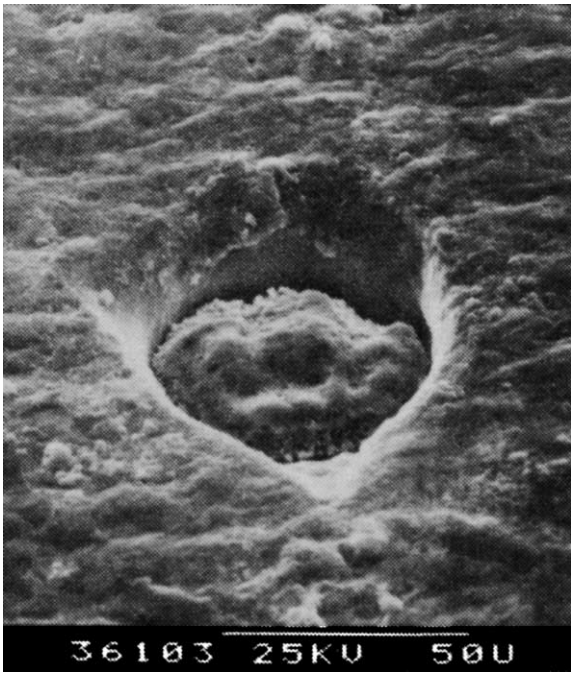

Fig. 9. SEM micrograph of LACE formed surface morphology of Ni (80%)–Fe (20%). Etching by CCl_4 at 100 Torr was driven by a 120 s pulse, focused Ar laser beam (taken from Ref. [23]). This picture shows that deeper etching has occurred at the edges—possibly due to thermally driven inhomogeneities within the CCl_4 that result in variations to the initially Gaussian beam profile.

quantitative analysis of LACE processing with materials such as BSG should include temperature dependent thermal and optical properties, temporally and spatially varying process gas density at surface and the interaction between the incident and reflected beam.

Acknowledgements

The authors wish to thank NSF for their support of this work. The work was supported by NSF Career grant number CTS-97-03402. Any opinions, findings, and conclusions or recommendations expressed in this publication are those of the authors and do not necessarily reflect the views of NSF. In addition, we would like to thank NCSA at UIUC for use of the supercomputer facilities in calculating the results.

References

[1] T.L. Chuang, Laser-induced chemical etching of solids: promises and challenges, in: A.W. Johnson, D.J. Ehrlich, H.R. Schlossberg (Eds.), Laser-Controlled Chemical Processing of Surfaces, North-Holland, New York, 1984, pp. 185–194.

[2] F.A. Houle, Laser-assisted chemical etching, in: S.D. Allen (Ed.), Laser Assisted Deposition, Etching, and Doping: January 26–27, 1984, Los Angeles, California, SPIE—The International Society for Optical Engineering, Bellingham, WA, 1984, pp. 110–114.

[3] J.J. Ritsko, Laser etching, in: D.J. Ehrlich, J.Y. Tsao (Eds.), Laser Microfabrication: Thin Film Processes and Lithography, Academic Press, Boston, 1989, pp. 333–383.
[4] D. Burgess Jr., P.C. Stair, E. Weitz, Calculations of the surface temperature rise and desorption temperature in laser-induced thermal desorption, J. Vac. Sci. Technol. A 4 (3) (1996) 1362–1366.
[5] J.M. Philippoz, R. Zenobi, R.N. Zare, Pulsed heating of surfaces: Comparison between numerical simulation, analytical models, and experiments, Chem. phys. lett. 158 (1,2) (1989) 12–16.
[6] O.O. Diniz Neto, C.A.S. Lima, Nonlinear three-dimensional temperature profiles in pulsed laser heated solids, J. Phys. D, Appl. Phys. 27 (9) (1994) 1795–1804.
[7] M. Lax, Temperature rise induced by a laser beam, J. Appl. Phys. 48 (9) (1977) 3919–3929.
[8] A. Maruani, Y.I. Nissim, F. Bonnouvrier, D. Paquet, Transients in CW laser heating of semiconductors: general method, analytical solutions and illustrations, J. Phys., Coll. 44 (C-5) (1983) 87–90.
[9] J.S. Hammonds Jr., M.A. Shannon, C. Li, Spatial output field for arbitrary input light field in a thermally self-induced inhomogeneous medium, Opt. Commun. 194 (1–3) (2001) 47–57.
[10] J.S. Hammonds Jr., Predicting the spatial output field of a laser beam in a thermally self-induced inhomogeneous medium, Ph.D. thesis, University of Illinois, Urbana, Illinois (2002).
[11] D. Bauerle, B. Luk'yanchuk, K. Piglmayer, On the reaction kinetics in laser-induced pyrolytic chemical processing, Appl. Phys. A, Solids Surf., A 50 (4) (1990) 385–396.
[12] R.B. Gold, J.F. Gibbons, Calculation of solid-phase reaction rates induced by a scanning CW laser, J. Appl. Phys. 51 (2) (1980) 1256–1258.
[13] M. Wautelet, On the influence of thermal history on simple surface reactions, J. Appl. Phys. 72 (7) (1992) 3091–3094.
[14] M.J. Madou, in: Fundamentals of Microfabrication, CRC Press, New York, 1997, pp. 183–185.
[15] J.S. Hammonds, F. Saied, M.A. Shannon, Solving the coupled 3-D paraxial wave equation and 3-D thermal diffusion equations with mixed-mode parallel computations, Parallel Comput., in press.
[16] P.J. Linstrom, W.G. Mallard (Eds.), NIST Chemistry WebBook, NIST Standard Reference Database Number 69, National Institute of Standards and Technology, Gaithersburg, 2001. Available from <http://webbook.nist. gov>.
[17] N. Kirichenko, K. Piglmayer, D. Bauerle, On the kinetics of nonequimolecular reactions in laser chemical processing, Appl. Phys. A, Solids Surf., A 51 (6) (1990) 498–507.
[18] R.E. Sonntag, G.J. Van Wylen, in: Introduction to Thermodynamics: Classical and Statistical, 3rd ed., Wiley, New York, 1991, pp. 440–451.
[19] Y. Tomkiewicz, E.L. Garwin, Optical absorption spectra of some potentially interesting gases for Cherenkov counters, Nucl. Instr. Meth. 114 (3) (1974) 413–416.
[20] D.R. Lide (Ed.), CRC Handbook of Chemistry and Physics, CRC Press, Boca Raton, 2000.
[21] Y.S. Touloukian, M. Tadashi (Eds.), Thermophysical Properties of Matter, IFI/Plenum, New York, 1970.
[22] W.A. Pliskin, The stability of glazed silicon surfaces to water attack, Proc. IEEE 52 (1964) 1468–1471.
[23] T.L. Chuang, Laser chemical etching of conducting and semiconducting materials, in: R.M. Osgood, S.R.J. Brueck, H.R. Schlossberg (Eds.), Laser Diagnostics and Photochemical Processing for Semiconductor Devices, North-Holland, New York, 1983, pp. 45–56.
[24] M. Takai, J. Tokuda, H. Nakai, K. Gamo, S. Namba, Laser induced local etching of gallium arsenide in gas atmosphere, Jn. J. Appl. Phys. Part 2, Lett. 22 (1983) L757–L759.